Rahman, F M Mahafugur; Pirsto, Ville; Kukkola, Jarno; Hinkkanen, Marko; Pérez-Estévez, Diego; Doval-Gandoy, Jesús

Equivalence of the integrator-based and disturbance-observer-based state-space current controllers for grid converters

Published in:
IEEE Transactions on Industrial Electronics

DOI:
10.1109/TIE.2020.2988194

Published: 01/06/2021

Document Version
Peer reviewed version

Please cite the original version:
Rahman, F. M. M., Pirsto, V., Kukkola, J., Hinkkanen, M., Pérez-Estévez, D., & Doval-Gandoy, J. (2021). Equivalence of the integrator-based and disturbance-observer-based state-space current controllers for grid converters. *IEEE Transactions on Industrial Electronics*, *68*(6), 4966-4976. [9075404]. https://doi.org/10.1109/TIE.2020.2988194

Equivalence of the Integrator-Based and Disturbance-Observer-Based State-Space Current Controllers for Grid Converters

F. M. Mahafugur Rahman, *Student Member, IEEE*, Ville Pirsto, Jarno Kukkola, Marko Hinkkanen, *Senior Member, IEEE*, Diego Pérez-Estévez, *Student Member, IEEE*, and Jesús Doval-Gandoy, *Member, IEEE*

***Abstract*—This paper deals with discrete-time state-space current controllers for three-phase grid converters equipped with an LCL filter. The integral action in the controller can be implemented either using an integrator or a disturbance observer. The results show that the disturbance-observer-based and integrator-based controllers become mathematically equal if the feedforward gains are selected to be equal, the feedforward zero is placed to cancel the pole originating from the integral action, and the closed-loop poles are placed identically. The equivalent performance in both designs is verified by means of analyses and experiments. The equivalence is also shown for double-frequency current controllers.**

***Index Terms*—Disturbance observer, double-frequency controller, grid converter, integrator, state-space current control.**

I. Introduction

CURRENT control plays a key role in modern power-electronic-based AC systems. In the last two decades, several hundreds of IEEE journal articles have been published on current control of grid converters equipped with an LCL filter. Among them, proportional-integral (PI) [1]–[4], proportional-resonant (PR) [3]–[6], and state-space [7]–[13] current controllers are very common. The synchronous-frame PI controller is found to be equivalent to the stationary-frame PR controller, i.e., both controllers yield same transient and steady-state performance [3]–[5]. Furthermore, PI control is a special case of state-space control with reference feedforward and integral action [14]. With an LCL filter, current control often includes an active resonance damping mechanism, e.g., [15]–[17].

A time delay in the current-control loop affects the system stability, particularly if an LCL filter is used. Due to the delay, the stability of current control depends on the ratio between the filter resonance frequency and the sampling frequency [2], [18], [19]. For example, single-loop grid-current PI control is unstable if the resonance frequency of the LCL filter is below one sixth of the sampling frequency, as shown in [17], [19], [20]. On the contrary, state-space control can stabilize the system independently of the filter resonance frequency, and it inherently enables active resonance damping [9].

In state-space control, the closed-loop dynamics can be set through pole-placement methods by selecting the closed-loop poles directly [8]–[10] or using linear quadratic (LQ) optimal control [21]–[23]. The direct discrete-time design improves pole-placement accuracy in the case of low sampling frequencies, resulting in superior performance as compared to the continuous-time design [8], [24]. In addition, the intrinsic delays of the digital implementation and pulse-width modulator (PWM) can be easily taken into account in the direct discrete-time design approach [8], [9].

The integral action in state-space control can be implemented in two ways [25]: integral control by state augmentation or disturbance estimation using an observer. In the former case, the integral action is included in the control law, whereas in the latter case, the integral action is a part of the state observer. Both control structures have been used in grid converters [8]–[10]. However, the links between these two apparently different structures are not yet well understood in the context of grid converters. Closely related to these structures, disturbance or uncertainty estimation methods [26] together with the state feedback have also been applied in [27], [28].

In this paper, we develop a common framework for both the integrator-based and disturbance-observer-based state-space current controllers for three-phase grid converters. The direct discrete-time design approach is selected. The main contribution of this paper is to show the equivalence of the integrator-based and disturbance-observer-based state-space current controllers in the context of grid converters. Furthermore, a design example for controller tuning is given. The equivalence of the control methods is extended for double-frequency current controllers. Both state-space controllers are evaluated by means of experiments using a three-phase 12.5-kVA grid converter.

II. System Model

A standard three-phase three-wire grid converter system is considered. Since there is no path for zero-sequence current

Manuscript received November 18, 2019; revised February 14, 2020 and March 10, 2020; accepted April 05, 2020. This work was supported in part by ABB Oy, in part by the Finnish Foundation for Technology Promotion, and in part by the Walter Ahlström Foundation.

F. M. M. Rahman, V. Pirsto, J. Kukkola, and M. Hinkkanen are with the Department of Electrical Engineering and Automation, Aalto University, Espoo, Finland (e-mail: f.rahman@aalto.fi; ville.pirsto@aalto.fi; jarno.kukkola@aalto.fi; marko.hinkkanen@aalto.fi).

D. Pérez-Estévez and J. Doval-Gandoy are with the Applied Power Electronics Technology Research Group, University of Vigo, Vigo, Spain (e-mail: dieperez@uvigo.es; jdoval@uvigo.es).

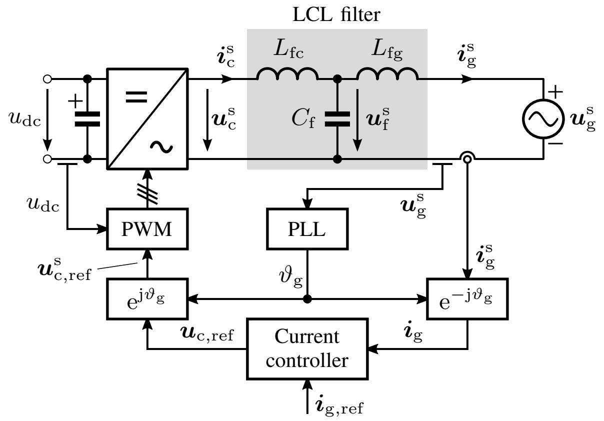

Fig. 1. Space-vector model of an LCL filter in stationary coordinates (vectors marked with the superscript s). The current controller, operating in grid-voltage coordinates, is also shown. The PLL determines the grid-voltage angle $\vartheta_{\rm g}$.

to flow, the zero-sequence components are omitted in the modeling [29]. Complex space vectors in synchronous dq coordinates are used to describe the system, e.g., the grid current is $\boldsymbol{i}_{\rm g} = i_{\rm gd} + \mathrm{j}i_{\rm gq}$. Complex-valued quantities are marked with boldface italic symbols, state vectors with boldface lowercase symbols, and system matrices with boldface uppercase symbols.

Fig. 1 shows a space-vector circuit model of the LCL filter. The converter voltage is denoted by $\boldsymbol{u}_{\rm c}$, the voltage across the capacitor by $\boldsymbol{u}_{\rm f}$, and the grid voltage by $\boldsymbol{u}_{\rm g}$. The converter current is $\boldsymbol{i}_{\rm c}$ and the LCL filter parameters are $L_{\rm fc}$, $C_{\rm f}$, and $L_{\rm fg}$. The undamped resonance angular frequency of the filter is

$$\omega_{\rm r} = \sqrt{\frac{L_{\rm fc}+L_{\rm fg}}{L_{\rm fc}C_{\rm f}L_{\rm fg}}}. \tag{1}$$

In synchronous dq coordinates rotating at the grid angular frequency $\omega_{\rm g}$, the dynamics of the grid current are

$$\begin{aligned} \mathbf{x}(k+1) &= \mathbf{\Phi}\mathbf{x}(k) + \mathbf{\Gamma}_{\rm c}\boldsymbol{u}_{\rm c,ref}(k) + \mathbf{\Gamma}_{\rm g}\boldsymbol{u}_{\rm g}(k) \\ \boldsymbol{i}_{\rm g}(k) &= \mathbf{C}_{\rm g}\mathbf{x}(k) \end{aligned} \tag{2}$$

where $\mathbf{x} = [\boldsymbol{i}_{\rm g}, \boldsymbol{i}_{\rm c}, \boldsymbol{u}_{\rm f}, \boldsymbol{u}_{\rm c}]^{\rm T}$ is the state vector and $\boldsymbol{u}_{\rm c,ref}$ is the converter voltage reference. The system matrices $\mathbf{\Phi}$, $\mathbf{\Gamma}_{\rm c}$, $\mathbf{\Gamma}_{\rm g}$, and $\mathbf{C}_{\rm g}$ are given in Appendix A. The plant model (2) relates the grid current to the converter voltage reference and the grid voltage. The model can be expressed also in the form of transfer functions,

$$\boldsymbol{Y}_{\rm c}(z) = \frac{\boldsymbol{i}_{\rm g}(z)}{\boldsymbol{u}_{\rm c,ref}(z)} = \mathbf{C}_{\rm g}(z\mathbf{I}-\mathbf{\Phi})^{-1}\mathbf{\Gamma}_{\rm c} \tag{3}$$

$$\boldsymbol{Y}_{\rm g}(z) = \frac{\boldsymbol{i}_{\rm g}(z)}{\boldsymbol{u}_{\rm g}(z)} = \mathbf{C}_{\rm g}(z\mathbf{I}-\mathbf{\Phi})^{-1}\mathbf{\Gamma}_{\rm g} \tag{4}$$

where $\mathbf{I}$ is the identity matrix.

III. Current Control

Fig. 1 shows the overall block diagram of the current control system. Only the grid current is needed for state-feedback control. The DC-link voltage $u_{\rm dc}$ is measured for the PWM and the grid voltage is measured for the phase-locked loop (PLL). The current controller operates in grid-voltage coordinates, where $\boldsymbol{u}_{\rm g} = u_{\rm g} + \mathrm{j}0$.

A. Integrator-Based Control

1) Control Law: Fig. 2(a) shows the integrator-based current control structure [8], [10], i.e., the control law is

$$\begin{aligned} \boldsymbol{x}_{\rm i}(k+1) &= \boldsymbol{x}_{\rm i}(k) + \boldsymbol{i}_{\rm g,ref}(k) - \boldsymbol{i}_{\rm g}(k) \\ \boldsymbol{u}_{\rm c,ref}(k) &= \boldsymbol{k}_{\rm t}\boldsymbol{i}_{\rm g,ref}(k) - \mathbf{K}_{\rm fi}\hat{\mathbf{x}}(k) + \boldsymbol{k}_{\rm i}\boldsymbol{x}_{\rm i}(k) \end{aligned} \tag{5}$$

where $\boldsymbol{k}_{\rm t}$ is the feedforward gain, $\mathbf{K}_{\rm fi}$ is the state-feedback gain, $\boldsymbol{k}_{\rm i}$ is the integral gain, $\boldsymbol{x}_{\rm i}$ is the integral state, and $\hat{\mathbf{x}} = [\boldsymbol{i}_{\rm g}, \hat{\mathbf{x}}_{\rm r}^{\rm T}]^{\rm T}$ is the state vector consisting of the measured state $\boldsymbol{i}_{\rm g}$ and estimated states $\hat{\mathbf{x}}_{\rm r} = [\hat{\boldsymbol{i}}_{\rm c}, \hat{\boldsymbol{u}}_{\rm f}, \hat{\boldsymbol{u}}_{\rm c}]^{\rm T}$. The integral state $\boldsymbol{x}_{\rm i}$ in the control law (5) eliminates the steady-state control error. The reference feedforward produces an additional zero in the numerator polynomial of the reference-tracking transfer function [8]. The reference-feedforward zero can be placed at $\boldsymbol{z}_{\rm t}$ by choosing the feedforward gain as

$$\boldsymbol{k}_{\rm t} = \boldsymbol{k}_{\rm i}/(1-\boldsymbol{z}_{\rm t}). \tag{6}$$

The feedforward zero can be used to cancel one of the control poles. An anti-windup mechanism is necessary in the integrator-based controller. The realizable reference anti-windup, shown in Fig. 2(a), is typically preferred [30].

2) Observer: The unknown states are estimated using a reduced-order observer. For its design, the state vector $\mathbf{x}$ is split into the measured state $\boldsymbol{i}_{\rm g}$ and the states $\mathbf{x}_{\rm r} = [\boldsymbol{i}_{\rm c}, \boldsymbol{u}_{\rm f}, \boldsymbol{u}_{\rm c}]^{\rm T}$ to be estimated. The system model (2) becomes

$$\begin{bmatrix}\boldsymbol{i}_{\rm g}(k+1)\\ \mathbf{x}_{\rm r}(k+1)\end{bmatrix} = \underbrace{\begin{bmatrix}\boldsymbol{\phi}_{\rm aa} & \mathbf{\Phi}_{\rm ab}\\ \mathbf{\Phi}_{\rm ba} & \mathbf{\Phi}_{\rm bb}\end{bmatrix}}_{\mathbf{\Phi}} \begin{bmatrix}\boldsymbol{i}_{\rm g}(k)\\ \mathbf{x}_{\rm r}(k)\end{bmatrix} + \underbrace{\begin{bmatrix}0\\ \mathbf{\Gamma}_{\rm r}\end{bmatrix}}_{\mathbf{\Gamma}_{\rm c}} \boldsymbol{u}_{\rm c,ref}(k) \tag{7}$$

where $\boldsymbol{\phi}_{\rm aa}$, $\mathbf{\Phi}_{\rm ab}$, $\mathbf{\Phi}_{\rm ba}$, and $\mathbf{\Phi}_{\rm bb}$ are the submatrices of $\mathbf{\Phi}$ and $\mathbf{\Gamma}_{\rm r}$ is the submatrix of $\mathbf{\Gamma}_{\rm c}$, cf. (2).[1] The grid voltage $\boldsymbol{u}_{\rm g}$ is considered as an unknown disturbance. Following the standard approach [25], the reduced-order observer can be written as

$$\begin{aligned} \hat{\mathbf{x}}_{\rm r}(k) &= \mathbf{\Phi}_{\rm bb}\hat{\mathbf{x}}_{\rm r}(k-1) + \mathbf{\Phi}_{\rm ba}\boldsymbol{i}_{\rm g}(k-1) \\ &\quad + \mathbf{\Gamma}_{\rm r}\boldsymbol{u}_{\rm c,ref}(k-1) + \mathbf{K}_{\rm oi}\boldsymbol{e}_{\rm o}(k) \end{aligned} \tag{8}$$

$$\boldsymbol{e}_{\rm o}(k) = \boldsymbol{i}_{\rm g}(k) - \boldsymbol{\phi}_{\rm aa}\boldsymbol{i}_{\rm g}(k-1) - \mathbf{\Phi}_{\rm ab}\hat{\mathbf{x}}_{\rm r}(k-1) \tag{9}$$

where $\mathbf{K}_{\rm oi}$ is the observer gain, and $\boldsymbol{e}_{\rm o}$ is the estimation error of the current. Since the grid voltage is considered as an unknown disturbance, the estimation error is nonzero in the steady state. However, the internal dynamics of the estimated states are correctly presented.

B. Disturbance-Observer-Based Control

1) Control Law: Fig. 2(b) shows the disturbance-observer-based current control structure [9], [31]. The control scheme uses an estimated disturbance $\hat{\boldsymbol{w}}$ in the control law in order to reduce the effect of grid disturbances on the grid current. In accordance with Fig. 2(b), the control law is

$$\boldsymbol{u}_{\rm c,ref}(k) = \boldsymbol{k}_{\rm f}\boldsymbol{i}_{\rm g,ref}(k) - \mathbf{K}_{\rm fd}\hat{\mathbf{x}}(k) - \hat{\boldsymbol{w}}(k) \tag{10}$$

[1]The dimension of the submatrix $\boldsymbol{\phi}_{\rm aa}$ is 1×1, i.e., it is simply a complex number. Therefore, its notation differs from those of other submatrices, cf. Section II.

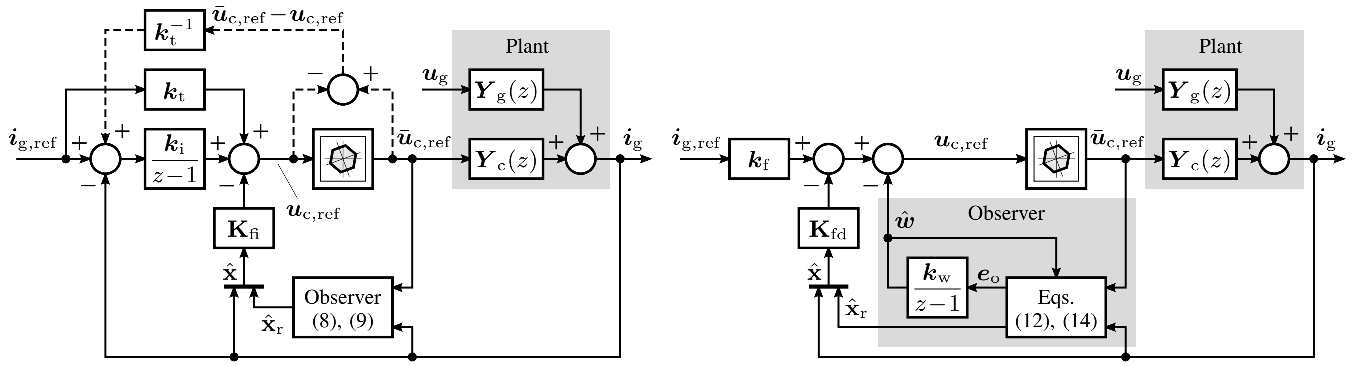

(a) (b)

Fig. 2. State-space current control with: (a) integrator; (b) disturbance observer. The realizable voltage reference $\bar{\boldsymbol{u}}_{\mathrm{c,ref}}$ can be calculated in the current controller or in the PWM, taking the converter-voltage saturation into account. In the linear modulation region, $\bar{\boldsymbol{u}}_{\mathrm{c,ref}} = \boldsymbol{u}_{\mathrm{c,ref}}$ holds. An anti-windup scheme, marked with the dashed lines in (a), is needed in the integrator-based controller.

where $\boldsymbol{k}_{\mathrm{f}}$ is the feedforward gain, $\mathbf{K}_{\mathrm{fd}}$ is the state-feedback gain, and $\hat{\mathbf{x}} = [\boldsymbol{i}_{\mathrm{g}}, \hat{\mathbf{x}}_{\mathrm{r}}^{\mathrm{T}}]^{\mathrm{T}}$ is the state vector, which contains both the measured state $\boldsymbol{i}_{\mathrm{g}}$ and estimated states $\hat{\mathbf{x}}_{\mathrm{r}} = [\hat{\boldsymbol{i}}_{\mathrm{c}}, \hat{\boldsymbol{u}}_{\mathrm{f}}, \hat{\boldsymbol{u}}_{\mathrm{c}}]^{\mathrm{T}}$. To achieve zero steady-state control error, the feedforward gain has to be chosen as

$$\boldsymbol{k}_{\mathrm{f}} = \frac{1}{\mathbf{C}_{\mathrm{g}}(\mathbf{I} - \boldsymbol{\Phi} + \boldsymbol{\Gamma}_{\mathrm{c}}\mathbf{K}_{\mathrm{fd}})^{-1}\boldsymbol{\Gamma}_{\mathrm{c}}}. \tag{11}$$

2) Observer: Since the grid voltage is considered as an unknown disturbance, an input-equivalent disturbance is used in this model, as explained in [9], [31]. The input-equivalent disturbance would produce the same effect on the grid current as the actual disturbance does [25]. The disturbance is assumed to be constant in synchronous dq coordinates. The observer is formulated based on the system model (7) and augmented with the disturbance state estimate, as

$$\begin{aligned}\hat{\mathbf{x}}_{\mathrm{r}}(k) &= \boldsymbol{\Phi}_{\mathrm{bb}}\hat{\mathbf{x}}_{\mathrm{r}}(k-1) + \boldsymbol{\Phi}_{\mathrm{ba}}\boldsymbol{i}_{\mathrm{g}}(k-1) \\ &\quad + \boldsymbol{\Gamma}_{\mathrm{r}}[\boldsymbol{u}_{\mathrm{c,ref}}(k-1) + \hat{\boldsymbol{w}}(k-1)] + \mathbf{K}_{\mathrm{od}}\boldsymbol{e}_{\mathrm{o}}(k) \quad (12)\\ \hat{\boldsymbol{w}}(k) &= \hat{\boldsymbol{w}}(k-1) + \boldsymbol{k}_{\mathrm{w}}\boldsymbol{e}_{\mathrm{o}}(k) \quad (13)\\ \boldsymbol{e}_{\mathrm{o}}(k) &= \boldsymbol{i}_{\mathrm{g}}(k) - \boldsymbol{\phi}_{\mathrm{aa}}\boldsymbol{i}_{\mathrm{g}}(k-1) - \boldsymbol{\Phi}_{\mathrm{ab}}\hat{\mathbf{x}}_{\mathrm{r}}(k-1) \quad (14)\end{aligned}$$

where $\mathbf{K}_{\mathrm{od}}$ and $\boldsymbol{k}_{\mathrm{w}}$ are the observer gains, and $\boldsymbol{e}_{\mathrm{o}}$ is the estimation error of the grid current. The disturbance state estimate $\hat{\boldsymbol{w}}$ is obtained by integrating the estimation error $\boldsymbol{e}_{\mathrm{o}}$. Due to the integral action, the estimation error becomes zero in the steady state.

C. Comparison of the Structures

In disturbance-observer-based control, the feedforward gain $\boldsymbol{k}_{\mathrm{f}}$ has a unique solution which results in zero steady-state control error. Differently, any value of the feedforward gain $\boldsymbol{k}_{\mathrm{t}}$ leads to zero steady-state control error in the integrator-based structure due to the integral action in the control law. The observer is of the third order in integrator-based control, whereas it is of the fourth order in disturbance-observer-based control. However, the order of the whole controller, including the observer and the control law, is the same in both structures. Unlike in integrator-based control, no additional anti-windup scheme is required in disturbance-observer-based control. Despite these structural differences, both controllers can have the same input-output behavior, as shown in the following sections.

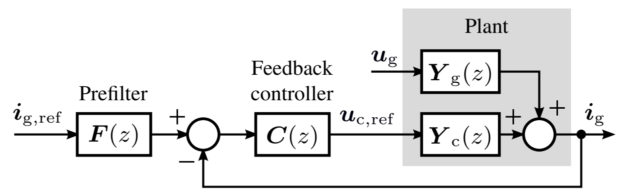

Fig. 3. 2DOF current control structure.

IV. Equivalence of the Controllers

In this section, we show that the integrator-based controller can be made mathematically equivalent to the disturbance-observer-based controller. First, a common framework for both controllers is developed. Then, the conditions for equivalence are derived.

A. Common Framework

Fig. 3 shows a common framework for two-degrees-of-freedom (2DOF) current controllers [32]. The framework consists of a feedback controller $\boldsymbol{C}(z)$, a reference prefilter $\boldsymbol{F}(z)$, and the open-loop transfer functions $\boldsymbol{Y}_{\mathrm{c}}(z)$ and $\boldsymbol{Y}_{\mathrm{g}}(z)$, given in (3) and (4). For simplicity, the converter voltage reference is assumed to stay in the linear modulation region. According to Fig. 3, the closed-loop response is

$$\boldsymbol{i}_{\mathrm{g}}(z) = \underbrace{\frac{\boldsymbol{F}(z)\boldsymbol{C}(z)\boldsymbol{Y}_{\mathrm{c}}(z)}{1 + \boldsymbol{C}(z)\boldsymbol{Y}_{\mathrm{c}}(z)}}_{\boldsymbol{G}(z)}\boldsymbol{i}_{\mathrm{g,ref}}(z) + \underbrace{\frac{\boldsymbol{Y}_{\mathrm{g}}(z)}{1 + \boldsymbol{C}(z)\boldsymbol{Y}_{\mathrm{c}}(z)}}_{\boldsymbol{Y}(z)}\boldsymbol{u}_{\mathrm{g}}(z) \tag{15}$$

where $\boldsymbol{G}(z)$ is the reference-tracking transfer function and $\boldsymbol{Y}(z)$ is the disturbance-rejection admittance. Both current controllers, shown in Fig. 2, can be presented in the framework of Fig. 3. The derivation of the transfer functions $\boldsymbol{C}(z)$ and $\boldsymbol{F}(z)$ is shown in Appendix B. To distinguish the controllers, the transfer functions and polynomials are marked with the superscript i for the integrator-based controller and with the superscript d for the disturbance-observer-based controller. For example, $\boldsymbol{C}(z)$ in integrator-based control is $\boldsymbol{C}^{\mathrm{i}}(z)$ and in disturbance-observer-based control is $\boldsymbol{C}^{\mathrm{d}}(z)$.

The characteristic polynomial of $\boldsymbol{G}(z)$ and $\boldsymbol{Y}(z)$ in (15) is denoted by $\boldsymbol{D}(z)$. Based on the separation principle [25], it can be written as

$$\boldsymbol{D}(z) = \boldsymbol{D}_{\mathrm{c}}(z)\boldsymbol{D}_{\mathrm{o}}(z) \tag{16}$$

where $\boldsymbol{D}_{\mathrm{c}}(z)$ is the control characteristic polynomial and $\boldsymbol{D}_{\mathrm{o}}(z)$ is the observer characteristic polynomial. In integrator based control, these polynomials are obtained from (2), (5), (8), and (9), and they are

$$\boldsymbol{D}_{\mathrm{c}}^{\mathrm{i}}(z) = \det\left(z\mathbf{I} - \begin{bmatrix} \boldsymbol{\Phi} & \mathbf{0} \\ -\mathbf{C}_{\mathrm{g}} & 1 \end{bmatrix} + \begin{bmatrix} \boldsymbol{\Gamma}_{\mathrm{c}} \\ 0 \end{bmatrix} \begin{bmatrix} \mathbf{K}_{\mathrm{fi}}, -\boldsymbol{k}_{\mathrm{i}} \end{bmatrix}\right) \tag{17}$$

$$\boldsymbol{D}_{\mathrm{o}}^{\mathrm{i}}(z) = \det(z\mathbf{I} - \boldsymbol{\Phi}_{\mathrm{bb}} + \mathbf{K}_{\mathrm{oi}}\boldsymbol{\Phi}_{\mathrm{ab}}). \tag{18}$$

In disturbance-observer-based control, the characteristic polynomials are obtained from (2), (10), and (12)−(14), and they are expressed as

$$\boldsymbol{D}_{\mathrm{c}}^{\mathrm{d}}(z) = \det(z\mathbf{I} - \boldsymbol{\Phi} + \boldsymbol{\Gamma}_{\mathrm{c}}\mathbf{K}_{\mathrm{fd}}) \tag{19}$$

$$\boldsymbol{D}_{\mathrm{o}}^{\mathrm{d}}(z) = \det\left(z\mathbf{I} - \begin{bmatrix} \boldsymbol{\Phi}_{\mathrm{bb}} & \boldsymbol{\Gamma}_{\mathrm{r}} \\ \mathbf{0} & 1 \end{bmatrix} + \begin{bmatrix} \mathbf{K}_{\mathrm{od}} \\ \boldsymbol{k}_{\mathrm{w}} \end{bmatrix} \begin{bmatrix} \boldsymbol{\Phi}_{\mathrm{ab}}, 0 \end{bmatrix}\right). \tag{20}$$

B. Conditions for Equivalence

The closed-loop systems, corresponding to Fig. 3, become equal for the same system if the following two conditions are met:

1) feedback controllers are equal, $\boldsymbol{C}^{\mathrm{i}}(z) = \boldsymbol{C}^{\mathrm{d}}(z)$;
2) reference prefilters are equal, $\boldsymbol{F}^{\mathrm{i}}(z) = \boldsymbol{F}^{\mathrm{d}}(z)$.

These conditions are further expressed in terms of characteristic polynomials of the systems in the following.

The structure of the plant (3) is of the form

$$\boldsymbol{Y}_{\mathrm{c}}(z) = \frac{\boldsymbol{P}(z)}{\boldsymbol{Q}(z)} = \frac{\boldsymbol{p}_2 z^2 + \boldsymbol{p}_1 z + \boldsymbol{p}_0}{z^4 + \boldsymbol{q}_3 z^3 + \boldsymbol{q}_2 z^2 + \boldsymbol{q}_1 z + \boldsymbol{q}_0}. \tag{21}$$

In both current controllers, the structure of the feedback controller is [cf. (51) and (56)]

$$\boldsymbol{C}(z) = \frac{\boldsymbol{A}(z)}{\boldsymbol{B}(z)} = \frac{\boldsymbol{a}_4 z^4 + \boldsymbol{a}_3 z^3 + \boldsymbol{a}_2 z^2 + \boldsymbol{a}_1 z + \boldsymbol{a}_0}{(z-1)(z^3 + \boldsymbol{b}_2 z^2 + \boldsymbol{b}_1 z + \boldsymbol{b}_0)}. \tag{22}$$

Using (21) and (22) in the closed-loop system (15), the characteristic polynomial can be written in the form of the Diophantine equation [31]

$$\boldsymbol{D}(z) = \boldsymbol{A}(z)\boldsymbol{P}(z) + \boldsymbol{B}(z)\boldsymbol{Q}(z). \tag{23}$$

By forming a system of linear equations of (23), it is observed that the solution of the coefficients of $\boldsymbol{A}(z)$ and $\boldsymbol{B}(z)$ for the characteristic polynomial $\boldsymbol{D}(z)$ is unique. Therefore, the feedback controllers become equal, $\boldsymbol{C}^{\mathrm{i}}(z) = \boldsymbol{C}^{\mathrm{d}}(z)$, if the characteristic polynomials of the two systems are identical,

$$\boldsymbol{D}^{\mathrm{i}}(z) = \boldsymbol{D}^{\mathrm{d}}(z). \tag{24}$$

The structure of the reference prefilter is [cf. (52) and (57)]

$$\boldsymbol{F}(z) = \frac{\boldsymbol{A}_{\mathrm{f}}(z)}{\boldsymbol{A}(z)} \tag{25}$$

where $\boldsymbol{A}_{\mathrm{f}}(z)$ is the numerator polynomial. As can be seen from (22) and (25), the denominator of $\boldsymbol{F}(z)$ is identical to the numerator of $\boldsymbol{C}(z)$. Therefore, if $\boldsymbol{C}^{\mathrm{i}}(z) = \boldsymbol{C}^{\mathrm{d}}(z)$, the denominators of $\boldsymbol{F}(z)$ in both current controllers are equal, $\boldsymbol{A}^{\mathrm{i}}(z) = \boldsymbol{A}^{\mathrm{d}}(z)$. Accordingly, the reference prefilters become equal, $\boldsymbol{F}^{\mathrm{i}}(z) = \boldsymbol{F}^{\mathrm{d}}(z)$, if the numerators of $\boldsymbol{F}(z)$

$$\boldsymbol{A}_{\mathrm{f}}^{\mathrm{i}}(z) = \boldsymbol{k}_{\mathrm{t}}(z - \boldsymbol{z}_{\mathrm{t}})\boldsymbol{D}_{\mathrm{o}}^{\mathrm{i}}(z) \tag{26}$$

$$\boldsymbol{A}_{\mathrm{f}}^{\mathrm{d}}(z) = \boldsymbol{k}_{\mathrm{f}}\boldsymbol{D}_{\mathrm{o}}^{\mathrm{d}}(z) \tag{27}$$

are equal in both controllers in addition to (24). The zero $\boldsymbol{z}_{\mathrm{t}} = 1 - \boldsymbol{k}_{\mathrm{i}}/\boldsymbol{k}_{\mathrm{t}}$ originates from the reference feedforward in integrator-based control, cf (6). In order to have equal reference prefilter $\boldsymbol{F}^{\mathrm{i}}(z) = \boldsymbol{F}^{\mathrm{d}}(z)$, the numerators of $\boldsymbol{F}(z)$ (26) and (27) further lead to the two conditions

$$\boldsymbol{k}_{\mathrm{f}} = \boldsymbol{k}_{\mathrm{t}} \tag{28}$$

$$\boldsymbol{D}_{\mathrm{o}}^{\mathrm{d}}(z) = (z - \boldsymbol{z}_{\mathrm{t}})\boldsymbol{D}_{\mathrm{o}}^{\mathrm{i}}(z). \tag{29}$$

According to (29), the feedforward zero has to be at the same location as one of the poles in $\boldsymbol{D}_{\mathrm{o}}^{\mathrm{d}}(z)$, and the rest of the poles in $\boldsymbol{D}_{\mathrm{o}}^{\mathrm{d}}(z)$ have to equal the poles in $\boldsymbol{D}_{\mathrm{o}}^{\mathrm{i}}(z)$. To summarize, the conditions (24), (28), and (29) have to be met for equivalent controllers. The equivalence of the two current controllers holds under any grid conditions or any parameter variations in the LCL filter.

TABLE I
NOMINAL PARAMETERS OF A 12.5-kVA CONVERTER SYSTEM

Parameter	Value	Value (p.u.)
LCL filter		
Converter-side inductance L_{fc}	3.3 mH	0.081
Grid-side inductance L_{fg}	3.0 mH	0.074
Capacitance C_{f}	8.8 μF	0.036
Grid		
Angular grid frequency ω_{g}	$2\pi\cdot$ 50 rad/s	1
Voltage (phase-neutral, peak)	$\sqrt{2/3}\cdot 400$ V	1
Converter		
Rated current (peak)	$\sqrt{2}\cdot 18$ A	1
DC-bus voltage u_{dc}	650 V	2

V. DESIGN EXAMPLE

In this section, a design example fulfilling the previous conditions is given. The parameters of a 12.5-kVA converter system, given in Table I, are used.

A. Pole Locations

The closed-loop poles are the roots of the characteristic polynomial $\boldsymbol{D}(z)$. They should be placed inside the unit circle in order to have a stable system. To fulfil the condition (24), the closed-loop poles are placed identically in both controllers using the direct pole-placement method [8]–[10]. In this design example, we choose the closed-loop pole locations by means of radial projection, i.e., the resonant open-loop poles of the LCL filter are damped but their resonance angular frequency is not altered [8]–[10]. The open-loop poles originating from the computational delay (located at $z = 0$) are not moved, since they are perfectly damped. Table II gives the selected pole locations, and Fig. 4 shows the locations in the complex plane. The control bandwidth α_{c} and the damping ratios (ζ_{r},

TABLE II
EXAMPLE CLOSED-LOOP POLE LOCATIONS

Poles	Location
Control	
Dominant	$\exp(-\alpha_c T_s)$
Complex conjugate resonant	$\exp\left[\left(-\zeta_r \pm j\sqrt{1-\zeta_r^2}\right)\omega_r T_s\right]$
Computational delay	0
Observer	
Complex conjugate resonant	$\exp\left[\left(-\zeta_o \pm j\sqrt{1-\zeta_o^2}\right)\omega_r T_s\right]$
Computational delay	0
Integral action	$\exp(-2\alpha_c T_s)$

TABLE III
DESIGN PARAMETERS

Parameter	Value	Value (p.u.)
Damping ratios ζ_r, ζ_o	0.7	
Control bandwidth α_c	$2\pi\cdot$ 400 rad/s	8
Sampling period T_s	125 μs	$2\pi\cdot$ 0.00625

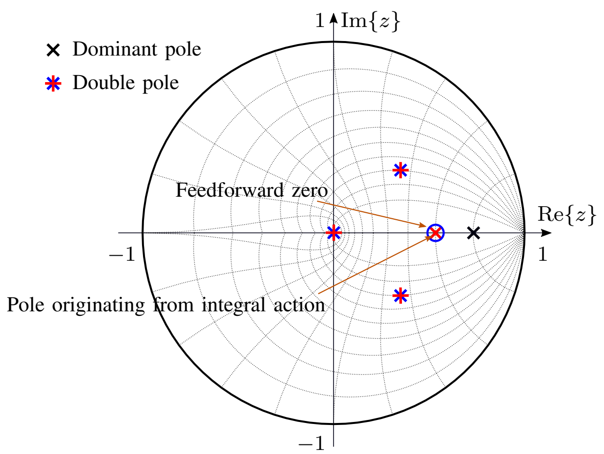

Fig. 4. Closed-loop poles, i.e., the roots of the characteristic polynomial $\boldsymbol{D}(z)$, under nominal conditions. They are obtained from Tables II and III. The blue circle shows the feedforward zero in the integrator-based control. The double poles originate from the computational delays and complex conjugate resonant poles.

ζ_o) are the design parameters, given in Table III. The dominant dynamics are determined by a real pole. The pole originating from the integral action is placed at twice the frequency of the dominant control pole.

In order to meet the condition in (29), the feedforward zero $\boldsymbol{z}_t$ of the integrator-based controller is placed at the same location as one of the observer poles in the disturbance-observer-based design. This selection of the feedforward zero leads to $\boldsymbol{k}_f = \boldsymbol{k}_t$, cf. (28). Using the defined pole locations, the controller and observer gains are calculated numerically, as described in [9], [10].

B. Closed-Loop Performance

Using (16), (24), and (29), the relation between the control characteristic polynomials becomes

$$\boldsymbol{D}_c^i(z) = (z - \boldsymbol{z}_t)\boldsymbol{D}_c^d(z). \tag{30}$$

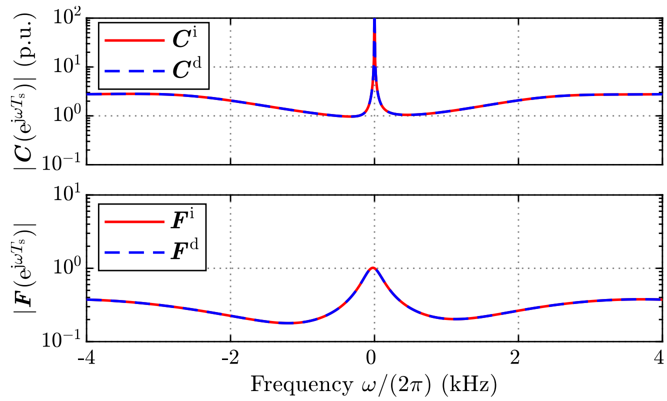

Fig. 5. Frequency responses of the current controllers: (above) feedback controller $\boldsymbol{C}(z)$, cf. (51) and (56); and (below) reference prefilter $\boldsymbol{F}(z)$, cf. (52) and (57). The superscript i marks the integrator-based controller and the superscript d marks the disturbance-observer-based controller.

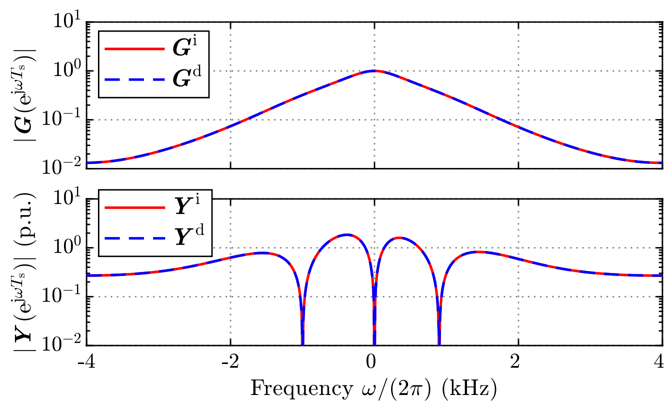

Fig. 6. Frequency responses of the closed-loop system in (15) under nominal conditions: (above) reference tracking $\boldsymbol{G}(z)$; and (below) disturbance rejection $\boldsymbol{Y}(z)$.

For integrator-based control, the reference-tracking transfer function can be derived from (2), (5), (8), and (9). Using (30), it can be expressed as

$$\boldsymbol{G}^i(z) = \frac{e^{-j\omega_g T_s}\boldsymbol{k}_t(z-\boldsymbol{z}_t)\boldsymbol{P}(z)}{\boldsymbol{D}_c^i(z)} = \frac{e^{-j\omega_g T_s}\boldsymbol{k}_t\boldsymbol{P}(z)}{\boldsymbol{D}_c^d(z)} \tag{31}$$

where T_s is the sampling period and $\boldsymbol{P}(z)$ is the numerator polynomial of $\boldsymbol{Y}_c(z)$, cf. (21). For disturbance-observer-based control, the reference-tracking transfer function is obtained from (2), (10), and (12)–(14)

$$\boldsymbol{G}^d(z) = \frac{e^{-j\omega_g T_s}\boldsymbol{k}_f\boldsymbol{P}(z)}{\boldsymbol{D}_c^d(z)}. \tag{32}$$

It can be seen that the transfer functions (31) and (32) do not depend on the observer under nominal conditions.[2]

Fig. 5 shows the frequency responses of the feedback controller $\boldsymbol{C}(z)$ and the reference prefilter $\boldsymbol{F}(z)$ for both controllers. As expected, the frequency responses of the two

[2]The poles and zeros of the transfer function originated from the observer are equal and thus pole-zero cancellation occurs [25]. Under parameter uncertainties, the poles of the observer move from their nominal locations. Then, pole-zero cancellation is not perfect and the transfer functions $\boldsymbol{G}^i(z)$ and $\boldsymbol{G}^d(z)$ also include both poles and zeros originated from the observer.

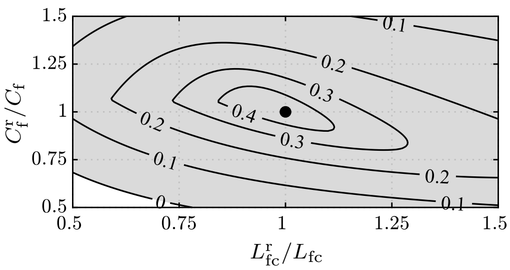

Fig. 7. Stability map in the presence of errors in the converter-side inductance L_{fc} and the filter capacitance C_{f}. The system is stable in the shaded area. The black dot shows the nominal conditions. The black lines show the contours of the lowest damping ratios (0, 0.1, 0.2, 0.3, and 0.4) of the eigenvalues.

controllers are equal. This equivalence holds independently of the filter parameter errors or grid conditions (if the same design parameters are used to parametrize both controllers). Fig. 6 shows the frequency responses for reference tracking $\boldsymbol{G}(z)$ and disturbance rejection $\boldsymbol{Y}(z)$, both defined in (15). To obtain these frequency responses, the open-loop transfer functions (3) and (4) together with the controller transfer functions (51) and (52) are used for integrator-based control. Analogously, the controller transfer functions (56) and (57) are used for disturbance-observer-based control. Naturally, these frequency responses are identical as well.

Fig. 7 shows an example of the robustness against the parameter errors in the LCL filter. The accurate system parameters are used in the control design. The real converter-side inductance $L_{\mathrm{fc}}^{\mathrm{r}}$ is varied in the range $L_{\mathrm{fc}}^{\mathrm{r}} = 0.5\ldots1.5L_{\mathrm{fc}}$ and the real filter capacitance $C_{\mathrm{f}}^{\mathrm{r}}$ is varied in the range $C_{\mathrm{f}}^{\mathrm{r}} = 0.5\ldots1.5C_{\mathrm{f}}$. It can be seen that the control systems tolerate errors in the LCL filter parameters. Due to equivalence, the robustness is same for both control systems. Furthermore, it is worth noticing that the performance and robustness depend on the selected pole locations.

VI. Double-Frequency Current Controllers

Both state-space control structures can be extended for double-frequency current control. The double-frequency controller controls the positive and negative sequences of the grid current. The reference current includes both the positive-sequence reference $\boldsymbol{i}_{\mathrm{g,ref+}}$ and the negative-sequence reference $\boldsymbol{i}_{\mathrm{g,ref-}}$, as shown in Fig. 8.

A. Integrator-Based Control

In integrator-based control, the controller needs two integrators to track the positive- and negative-sequence current references with zero steady-state control error. The double-frequency control law is

$$\begin{aligned}\boldsymbol{x}_{\mathrm{i+}}(k+1) &= \boldsymbol{x}_{\mathrm{i+}}(k) + \boldsymbol{i}_{\mathrm{g,ref+}}(k) - \boldsymbol{i}_{\mathrm{g}}(k) + \boldsymbol{k}_{\mathrm{ti-}}\boldsymbol{i}_{\mathrm{g,ref-}}(k)\\ \boldsymbol{x}_{\mathrm{i-}}(k+1) &= \mathrm{e}^{-2\mathrm{j}\omega_{\mathrm{g}}T_{\mathrm{s}}}\boldsymbol{x}_{\mathrm{i-}}(k) + \boldsymbol{i}_{\mathrm{g,ref-}}(k) - \boldsymbol{i}_{\mathrm{g}}(k)\\ &\quad + \boldsymbol{k}_{\mathrm{ti+}}\boldsymbol{i}_{\mathrm{g,ref+}}(k)\\ \boldsymbol{u}_{\mathrm{c,ref}}(k) &= \boldsymbol{k}_{\mathrm{t+}}\boldsymbol{i}_{\mathrm{g,ref+}}(k) + \boldsymbol{k}_{\mathrm{t-}}\boldsymbol{i}_{\mathrm{g,ref-}}(k)\\ &\quad + \boldsymbol{k}_{\mathrm{i+}}\boldsymbol{x}_{\mathrm{i+}}(k) + \boldsymbol{k}_{\mathrm{i-}}\boldsymbol{x}_{\mathrm{i-}}(k) - \mathbf{K}_{\mathrm{fi}}\hat{\mathbf{x}}(k)\end{aligned} \tag{33}$$

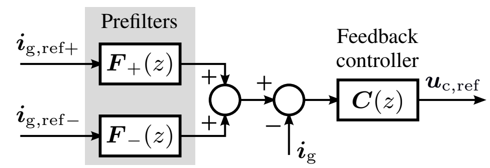

Fig. 8. 2DOF representation of a double-frequency current controller.

where $\boldsymbol{x}_{\mathrm{i+}}$ and $\boldsymbol{x}_{\mathrm{i-}}$ are the integral states, $\boldsymbol{k}_{\mathrm{t+}}$ and $\boldsymbol{k}_{\mathrm{t-}}$ are the feedforward gains, and $\boldsymbol{k}_{\mathrm{i+}}$ and $\boldsymbol{k}_{\mathrm{i-}}$ are the integral gains for the positive and negative sequences, respectively. The gains $\boldsymbol{k}_{\mathrm{ti+}}$ and $\boldsymbol{k}_{\mathrm{ti-}}$ are needed to eliminate the coupling between the positive- and negative-sequence reference chains.

The control law (33) together with the system model (2) leads to the control characteristic polynomial

$$\boldsymbol{D}_{\mathrm{c}}^{\mathrm{i}}(z) = \det\left(z\mathbf{I} - \begin{bmatrix}\mathbf{\Phi} & \mathbf{0} & \mathbf{0}\\ -\mathbf{C}_{\mathrm{g}} & 1 & 0\\ -\mathbf{C}_{\mathrm{g}} & 0 & \mathrm{e}^{-2\mathrm{j}\omega_{\mathrm{g}}T_{\mathrm{s}}}\end{bmatrix} + \begin{bmatrix}\mathbf{\Gamma}_{\mathrm{c}}\\ 0\\ 0\end{bmatrix}\mathbf{K}_{\mathrm{fi}}'\right) \tag{34}$$

where $\mathbf{K}_{\mathrm{fi}}' = \left[\mathbf{K}_{\mathrm{fi}}, -\boldsymbol{k}_{\mathrm{i+}}, -\boldsymbol{k}_{\mathrm{i-}}\right]$. The observer characteristic polynomial $\boldsymbol{D}_{\mathrm{o}}^{\mathrm{i}}(z)$ is the same as (18). The gains $\boldsymbol{k}_{\mathrm{t+}}$ and $\boldsymbol{k}_{\mathrm{ti+}}$ introduce two feedforward zeros in the positive-sequence reference-tracking transfer function $\boldsymbol{G}_{+}^{\mathrm{i}}(z) = \boldsymbol{i}_{\mathrm{g}}(z)/\boldsymbol{i}_{\mathrm{g,ref+}}(z)$. Under nominal conditions, the transfer function is obtained from (2) and (33), as

$$\boldsymbol{G}_{+}^{\mathrm{i}}(z) = \frac{\mathrm{e}^{-\mathrm{j}\omega_{\mathrm{g}}T_{\mathrm{s}}}\boldsymbol{k}_{\mathrm{t+}}(z-\boldsymbol{z}_{\mathrm{t}})(z-\boldsymbol{z}_{\mathrm{ti}})\boldsymbol{P}(z)}{\boldsymbol{D}_{\mathrm{c}}^{\mathrm{i}}(z)}. \tag{35}$$

The feedforward zeros $\boldsymbol{z}_{\mathrm{t}}$ and $\boldsymbol{z}_{\mathrm{ti}}$ can be used for pole-zero cancellation and decoupling of the positive- and negative-sequence reference chains. The feedforward zeros are placed on top of the integral-action originated poles in a similar manner as in the case of the single-frequency controller, cf. Fig. 4. The feedforward and decoupling gains

$$\begin{aligned}\boldsymbol{k}_{\mathrm{t+}} &= \frac{\boldsymbol{k}_{\mathrm{i+}}(1-\mathrm{e}^{-2\mathrm{j}\omega_{\mathrm{g}}T_{\mathrm{s}}})}{1-\boldsymbol{z}_{\mathrm{t}}-\boldsymbol{z}_{\mathrm{ti}}+\boldsymbol{z}_{\mathrm{t}}\boldsymbol{z}_{\mathrm{ti}}}\\ \boldsymbol{k}_{\mathrm{ti+}} &= \frac{\boldsymbol{k}_{\mathrm{i+}}\mathrm{e}^{-2\mathrm{j}\omega_{\mathrm{g}}T_{\mathrm{s}}}(\boldsymbol{z}_{\mathrm{t}}+\boldsymbol{z}_{\mathrm{ti}}-\mathrm{e}^{-2\mathrm{j}\omega_{\mathrm{g}}T_{\mathrm{s}}}-\boldsymbol{z}_{\mathrm{t}}\boldsymbol{z}_{\mathrm{ti}}\mathrm{e}^{2\mathrm{j}\omega_{\mathrm{g}}T_{\mathrm{s}}})}{\boldsymbol{k}_{\mathrm{i-}}(1-\boldsymbol{z}_{\mathrm{t}}-\boldsymbol{z}_{\mathrm{ti}}+\boldsymbol{z}_{\mathrm{t}}\boldsymbol{z}_{\mathrm{ti}})}\end{aligned} \tag{36}$$

are obtained analytically as a function of the integral gains and feedforward zeros.

Similarly, the gains $\boldsymbol{k}_{\mathrm{t-}}$ and $\boldsymbol{k}_{\mathrm{ti-}}$ produce two feedforward zeros in the negative-sequence reference-tracking transfer function $\boldsymbol{G}_{-}^{\mathrm{i}}(z) = \boldsymbol{i}_{\mathrm{g}}(z)/\boldsymbol{i}_{\mathrm{g,ref-}}(z)$. The feedforward zeros are placed at the same locations as the integral-action originated poles. The analytical expressions for the feedforward and decoupling gains are

$$\begin{aligned}\boldsymbol{k}_{\mathrm{t-}} &= \frac{\boldsymbol{k}_{\mathrm{i-}}(1-\mathrm{e}^{2\mathrm{j}\omega_{\mathrm{g}}T_{\mathrm{s}}})}{\mathrm{e}^{-2\mathrm{j}\omega_{\mathrm{g}}T_{\mathrm{s}}}-\boldsymbol{z}_{\mathrm{t}}-\boldsymbol{z}_{\mathrm{ti}}+\boldsymbol{z}_{\mathrm{t}}\boldsymbol{z}_{\mathrm{ti}}\mathrm{e}^{2\mathrm{j}\omega_{\mathrm{g}}T_{\mathrm{s}}}}\\ \boldsymbol{k}_{\mathrm{ti-}} &= \frac{\boldsymbol{k}_{\mathrm{i-}}\mathrm{e}^{2\mathrm{j}\omega_{\mathrm{g}}T_{\mathrm{s}}}(\boldsymbol{z}_{\mathrm{t}}+\boldsymbol{z}_{\mathrm{ti}}-1-\boldsymbol{z}_{\mathrm{t}}\boldsymbol{z}_{\mathrm{ti}})}{\boldsymbol{k}_{\mathrm{i+}}(\mathrm{e}^{-2\mathrm{j}\omega_{\mathrm{g}}T_{\mathrm{s}}}-\boldsymbol{z}_{\mathrm{t}}-\boldsymbol{z}_{\mathrm{ti}}+\boldsymbol{z}_{\mathrm{t}}\boldsymbol{z}_{\mathrm{ti}}\mathrm{e}^{2\mathrm{j}\omega_{\mathrm{g}}T_{\mathrm{s}}})}.\end{aligned} \tag{37}$$

The rest of the design of the control method is similar to the design explained in Section III-A.

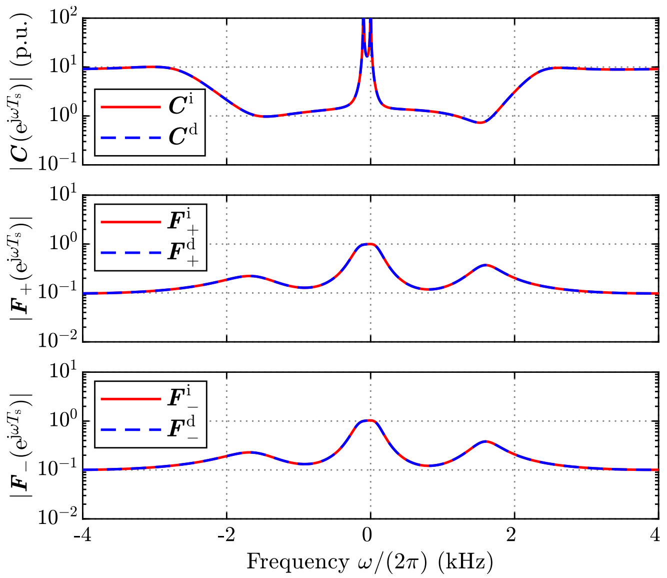

Fig. 9. Frequency responses of the double-frequency controllers: (top) feedback controller $\boldsymbol{C}(z)$; (middle) positive-sequence reference prefilter $\boldsymbol{F}_+(z)$; and (bottom) negative-sequence reference prefilter $\boldsymbol{F}_-(z)$.

B. Disturbance-Observer-Based Control

In disturbance-observer-based control, both positive and negative sequences of the grid voltage are considered to be a disturbance for the current controller. Thus, the hold-equivalent disturbance model becomes

$$\begin{aligned}\mathbf{r}(k+1) &= \begin{bmatrix}1 & 0\\ 0 & \mathrm{e}^{-2\mathrm{j}\omega_\mathrm{g}T_\mathrm{s}}\end{bmatrix}\mathbf{r}(k)\\ \boldsymbol{w}_\mathrm{d}(k) &= \begin{bmatrix}1 & 1\end{bmatrix}\mathbf{r}(k)\end{aligned} \tag{38}$$

where $\mathbf{r} = [\boldsymbol{w}_+, \boldsymbol{w}_-]^\mathrm{T}$ is the disturbance state vector consisting of the positive-sequence disturbance $\boldsymbol{w}_+$ and negative-sequence disturbance $\boldsymbol{w}_-$. This disturbance model is embedded into the observer analogously to (12). The control law is

$$\boldsymbol{u}_\mathrm{c,ref}(k) = \boldsymbol{k}_\mathrm{f+}\boldsymbol{i}_\mathrm{g,ref+}(k) + \boldsymbol{k}_\mathrm{f-}\boldsymbol{i}_\mathrm{g,ref-}(k) - \mathbf{K}_\mathrm{fd}\hat{\mathbf{x}}(k) - \hat{\boldsymbol{w}}_\mathrm{d}(k) \tag{39}$$

where $\boldsymbol{k}_\mathrm{f+}$ and $\boldsymbol{k}_\mathrm{f-}$ are the feedforward gains for the positive and negative sequences, respectively. The gain $\boldsymbol{k}_\mathrm{f+} = \boldsymbol{k}_\mathrm{f}$ is given in (11). To achieve zero steady-state control error for the negative sequence reference tracking, the feedforward gain has to be chosen as

$$\boldsymbol{k}_\mathrm{f-} = \frac{1}{\mathbf{C}_\mathrm{g}(\mathrm{e}^{-2\mathrm{j}\omega_\mathrm{g}T_\mathrm{s}}\mathbf{I} - \mathbf{\Phi} + \mathbf{\Gamma}_\mathrm{c}\mathbf{K}_\mathrm{fd})^{-1}\mathbf{\Gamma}_\mathrm{c}}. \tag{40}$$

Otherwise, the control design is similar to that explained in Section III-B. The control characteristic polynomial $\boldsymbol{D}_\mathrm{c}^\mathrm{d}(z)$ is obtained analogously to (19) and the observer characteristic polynomial $\boldsymbol{D}_\mathrm{o}^\mathrm{d}(z)$ analogously to (20).

C. Equivalence

Both double-frequency controllers can be shown equal in a similar manner as the single-frequency controllers, as explained in Section IV. They are equal if $\boldsymbol{k}_\mathrm{t+} = \boldsymbol{k}_\mathrm{f+}$, $\boldsymbol{k}_\mathrm{t-} = \boldsymbol{k}_\mathrm{f-}$, the feedforward zeros cancel the poles originating from the integral actions, and the closed-loop poles are identical. Fig. 9 shows the frequency responses of the feedback controller $\boldsymbol{C}(z)$ and the positive- and negative-sequence reference prefilters $\boldsymbol{F}_+(z)$ and $\boldsymbol{F}_-(z)$ for both current controllers. It can be seen that the controllers are equivalent. It is worth mentioning that the transfer functions $\boldsymbol{C}(z)$, $\boldsymbol{F}_+(z)$, and $\boldsymbol{F}_-(z)$ are obtained in an analogous manner as for the single-frequency controller given in Appendix B.

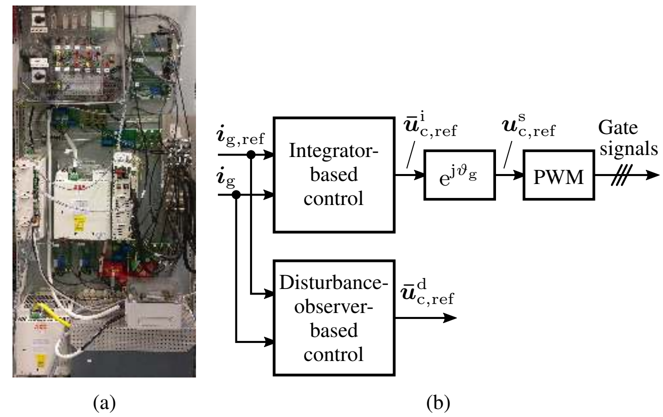

Fig. 10. Experimental setup: (a) photograph; and (b) schematic.

D. Comparison of the Structures

In disturbance-observer-based control, the feedforward gains $\boldsymbol{k}_\mathrm{f+}$ and $\boldsymbol{k}_\mathrm{f-}$ are calculated in a straightforward way using (11) and (40) to achieve zero steady-state control error for the positive and negative sequences, respectively. In integrator-based control, two additional gains $\boldsymbol{k}_\mathrm{ti+}$ and $\boldsymbol{k}_\mathrm{ti-}$ given in (36) and (37) are required to decouple the positive- and negative-sequence reference chains. In addition, integrator-based control requires an anti-windup mechanism for both positive and negative sequences, which leads to a more complex structure as compared to disturbance-observer-based control. No anti-windup scheme is needed in disturbance-observer-based control. Despite the structural differences, the controllers can be designed to be equal, as shown in Fig. 9.

VII. Experimental Results

The design example presented in Section V is evaluated by means of experiments using a 12.5-kVA 50-Hz grid converter. Fig. 10(a) shows a photograph of the experimental setup. The grid is emulated with a 50-kVA three-phase four-quadrant power supply (Regatron TopCon TC.ACS). A PLL having the bandwidth of $2\pi \cdot 2$ rad/s, operating in synchronous coordinates, is used [33]. The test converter controls the grid current and another back-to-back connected converter provides constant DC-link voltage. The switching frequency of the converter under test is 4 kHz and synchronous sampling (twice per carrier) is used.

As shown in Fig. 10(b), both current controllers were implemented in parallel, but, the converter is controlled using the gate signals produced by the integrator-based controller. Fig. 11 shows the measured responses of the grid current components i_gd and i_gq and equal control effort provided by

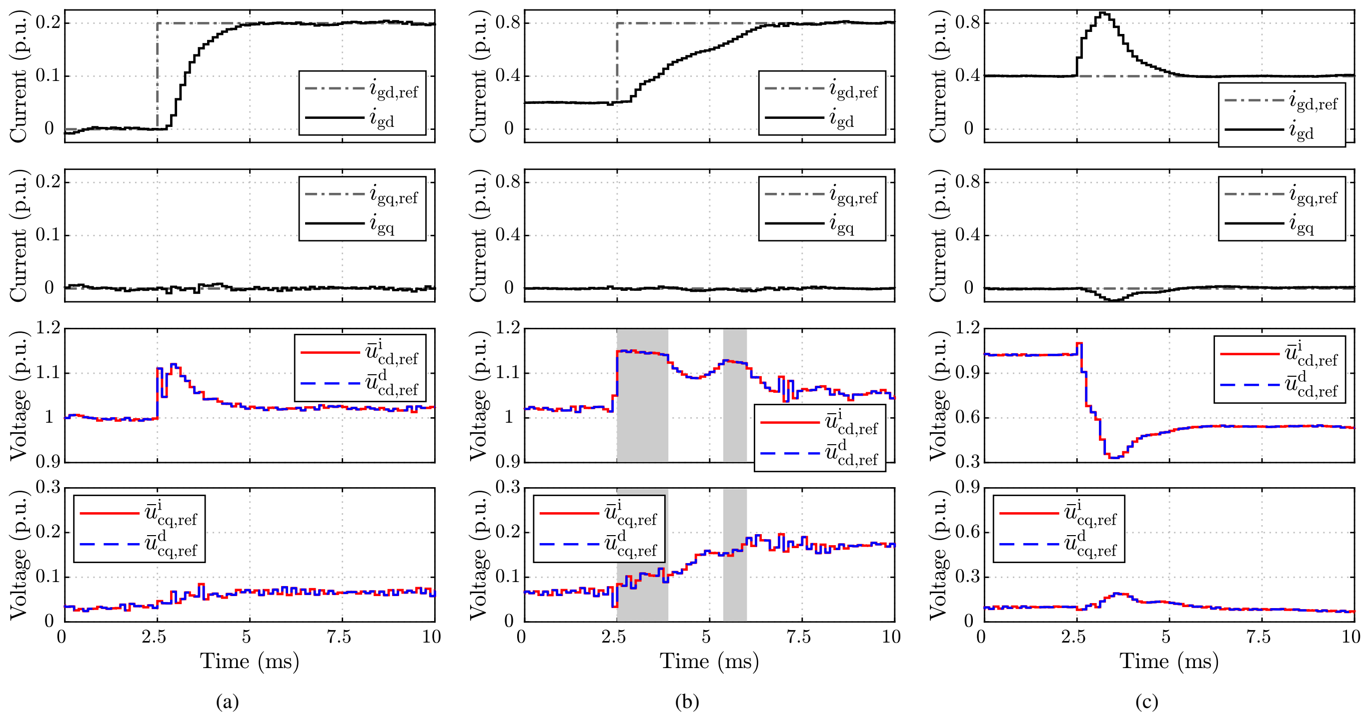

Fig. 11. Experimental results: (a) reference tracking in the linear modulation region; (b) reference tracking with the converter-voltage saturation; and (c) disturbance rejection against the grid-voltage dip. In (b), the converter voltage saturates in the shaded regions.

both controllers, i.e., $\bar{u}^{\mathrm{i}}_{\mathrm{cd,ref}} = \bar{u}^{\mathrm{d}}_{\mathrm{cd,ref}}$ and $\bar{u}^{\mathrm{i}}_{\mathrm{cq,ref}} = \bar{u}^{\mathrm{d}}_{\mathrm{cq,ref}}$. Due to the equal control effort, both controllers naturally lead to identical grid current responses.

Fig. 11(a) shows the measured responses, when a current reference step of 0.2 p.u is applied to $i_{\mathrm{gd,ref}}$. A small reference step is chosen in order to keep the converter voltage reference in the linear modulation region. As can be observed, the converter voltage stays in the linear modulation region, $\bar{\boldsymbol{u}}_{\mathrm{c,ref}} = \boldsymbol{u}_{\mathrm{c,ref}}$ holds, corresponding to the analysis shown in Section IV. Fig. 11(b) shows the measured responses for a current reference step of 0.6 p.u. Due to the large reference step, the converter voltage saturates. In this case, the realizable voltage reference reaches the maximum available voltage $|\bar{\boldsymbol{u}}_{\mathrm{c,ref}}| = u_{\mathrm{dc}}/\sqrt{3}$, and thus $\bar{\boldsymbol{u}}_{\mathrm{c,ref}} \neq \boldsymbol{u}_{\mathrm{c,ref}}$. Fig. 11(c) shows the disturbance-rejection capability of the controllers in the case of a balanced grid-voltage dip. The converter supplies the power of 0.4 p.u. to the grid. A voltage dip of 0.5 p.u. is applied at 2.5 ms. As can be seen, the current controllers reject the grid-voltage dip well.

Fig. 12 shows the harmonic-disturbance rejection capability of the controllers. The fifth and seventh harmonic components of 0.03 p.u. are superimposed on the grid voltage at 20 ms. The converter supplies the power of 1 p.u. to the grid. The resulting fifth and seventh harmonic currents are 0.043 p.u. and 0.039 p.u., respectively. The total harmonic distortion (THD) of the grid current up to the 50th order is 1.4% and 5.9% without and with the imposed harmonic components, respectively.

VIII. Conclusion

We have shown that the disturbance-observer-based and integrator-based state-space current controllers become mathematically equal, if the closed-loop poles are placed identically, the feedforward gains are equal, and the feedforward zero cancels the pole originating from the integral action. The conditions for equivalence were extended to double-frequency current controllers as well. In this paper, the reduced-order observer was used as an example, but the equivalence conditions for the full-order observers can be obtained in an analogous manner. Similarly, the equivalence conditions could be derived for the controllers, whose feedback signal is the converter current, instead of the grid current used in this paper.

Appendix A
Discrete-Time System Model

A continuous-time model of the LCL filter in synchronous dq coordinates rotating at ω_{g} can be written as

$$\frac{\mathrm{d}\mathbf{x}_{\mathrm{p}}}{\mathrm{d}t} = \underbrace{\begin{bmatrix} -\mathrm{j}\omega_{\mathrm{g}} & 0 & \frac{1}{L_{\mathrm{fg}}} \\ 0 & -\mathrm{j}\omega_{\mathrm{g}} & -\frac{1}{L_{\mathrm{fc}}} \\ -\frac{1}{C_{\mathrm{f}}} & \frac{1}{C_{\mathrm{f}}} & -\mathrm{j}\omega_{\mathrm{g}} \end{bmatrix}}_{\mathbf{A}_{\mathrm{p}}} \mathbf{x}_{\mathrm{p}} + \underbrace{\begin{bmatrix} 0 \\ \frac{1}{L_{\mathrm{fc}}} \\ 0 \end{bmatrix}}_{\mathbf{B}_{\mathrm{c}}} \boldsymbol{u}_{\mathrm{c}} + \underbrace{\begin{bmatrix} -\frac{1}{L_{\mathrm{fg}}} \\ 0 \\ 0 \end{bmatrix}}_{\mathbf{B}_{\mathrm{g}}} \boldsymbol{u}_{\mathrm{g}} \tag{41}$$

where $\mathbf{x}_{\mathrm{p}} = \left[\boldsymbol{i}_{\mathrm{g}}, \boldsymbol{i}_{\mathrm{c}}, \boldsymbol{u}_{\mathrm{f}}\right]^{\mathrm{T}}$ is the state vector. The PWM is modeled as the zero-order hold (ZOH) in stationary coordinates. The grid current is sampled synchronously with the ZOH. Under these assumptions, the hold-equivalent discrete-time model of (41) becomes

$$\mathbf{x}_{\mathrm{p}}(k+1) = \mathbf{\Phi}_{\mathrm{p}}\mathbf{x}_{\mathrm{p}}(k) + \mathbf{\Gamma}_{\mathrm{cp}}\boldsymbol{u}_{\mathrm{c}}(k) + \mathbf{\Gamma}_{\mathrm{gp}}\boldsymbol{u}_{\mathrm{g}}(k) \tag{42}$$

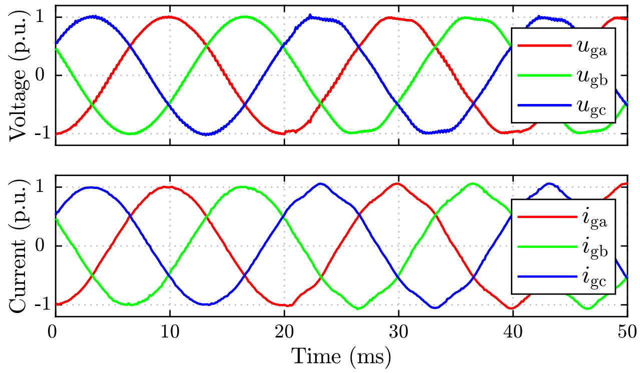

Fig. 12. Measured (above) grid phase voltages and (below) grid phase currents. The fifth and seventh harmonics are superimposed at 20 ms.

where the system matrices are [8]

$$\mathbf{\Phi}_{\rm p} = {\rm e}^{\mathbf{A}_{\rm p} T_{\rm s}} \qquad \mathbf{\Gamma}_{\rm cp} = \int_0^{T_{\rm s}} {\rm e}^{\mathbf{A}_{\rm p}\tau} {\rm e}^{-{\rm j}\omega_{\rm g}(T_{\rm s}-\tau)} {\rm d}\tau \cdot \mathbf{B}_{\rm c}$$
$$\mathbf{\Gamma}_{\rm gp} = \int_0^{T_{\rm s}} {\rm e}^{\mathbf{A}_{\rm p}\tau} {\rm d}\tau \cdot \mathbf{B}_{\rm g}. \tag{43}$$

The closed-form expressions of the system matrices (43) are

$$\mathbf{\Phi}_{\rm p} = \boldsymbol{\gamma} \begin{bmatrix} \frac{L_{\rm fg}+L_{\rm fc}\cos(\omega_{\rm r}T_{\rm s})}{L_{\rm fc}+L_{\rm fg}} & \frac{L_{\rm fc}[1-\cos(\omega_{\rm r}T_{\rm s})]}{L_{\rm fc}+L_{\rm fg}} & \frac{\sin(\omega_{\rm r}T_{\rm s})}{\omega_{\rm r}L_{\rm fg}} \\ \frac{L_{\rm fg}[1-\cos(\omega_{\rm r}T_{\rm s})]}{L_{\rm fc}+L_{\rm fg}} & \frac{L_{\rm fc}+L_{\rm fg}\cos(\omega_{\rm r}T_{\rm s})}{L_{\rm fc}+L_{\rm fg}} & -\frac{\sin(\omega_{\rm r}T_{\rm s})}{\omega_{\rm r}L_{\rm fc}} \\ -\frac{\sin(\omega_{\rm r}T_{\rm s})}{\omega_{\rm r}C_{\rm f}} & \frac{\sin(\omega_{\rm r}T_{\rm s})}{\omega_{\rm r}C_{\rm f}} & \cos(\omega_{\rm r}T_{\rm s}) \end{bmatrix}$$
$$\mathbf{\Gamma}_{\rm cp} = \frac{\boldsymbol{\gamma}}{L_{\rm fc}+L_{\rm fg}} \begin{bmatrix} T_{\rm s} - \frac{\sin(\omega_{\rm r}T_{\rm s})}{\omega_{\rm r}} \\ T_{\rm s} + \frac{L_{\rm fg}\sin(\omega_{\rm r}T_{\rm s})}{\omega_{\rm r}L_{\rm fc}} \\ L_{\rm fg}[1-\cos(\omega_{\rm r}T_{\rm s})] \end{bmatrix}$$
$$\mathbf{\Gamma}_{\rm gp} = \begin{bmatrix} \frac{\boldsymbol{\gamma}[\rho L_{\rm fc}\sin(\omega_{\rm r}T_{\rm s}) - {\rm j}\delta L_{\rm fg} - {\rm j}\omega_{\rm g}^2 L_{\rm fc}\cos(\omega_{\rm r}T_{\rm s})] + {\rm j}\delta L_{\rm fg} + {\rm j}\omega_{\rm g}^2 L_{\rm fc}}{\delta\omega_{\rm g}L_{\rm fg}(L_{\rm fc}+L_{\rm fg})} \\ \frac{\boldsymbol{\gamma}[-\rho\sin(\omega_{\rm r}T_{\rm s}) + {\rm j}\omega_{\rm g}^2\cos(\omega_{\rm r}T_{\rm s}) - {\rm j}\delta] - {\rm j}\omega_{\rm r}^2}{\delta\omega_{\rm g}(L_{\rm fc}+L_{\rm fg})} \\ \frac{\boldsymbol{\gamma}[\omega_{\rm r}\cos(\omega_{\rm r}T_{\rm s}) + {\rm j}\omega_{\rm g}\sin(\omega_{\rm r}T_{\rm s})] - \omega_{\rm r}}{\delta\omega_{\rm r}C_{\rm f}L_{\rm fg}} \end{bmatrix} \tag{44}$$

where $\boldsymbol{\gamma} = {\rm e}^{-{\rm j}\omega_{\rm g}T_{\rm s}}$, $\rho = \omega_{\rm g}\omega_{\rm r}$, and $\delta = \omega_{\rm g}^2 - \omega_{\rm r}^2$.

A computational delay of one sampling period exists in standard implementations [8], [9].[3] The effect of the computational delay can be modeled in synchronous dq coordinates as [8]

$$\boldsymbol{u}_{\rm c}(k+1) = \boldsymbol{\gamma}\boldsymbol{u}_{\rm c,ref}(k) \tag{45}$$

where $\boldsymbol{u}_{\rm c,ref}$ is the converter voltage reference. With this delay, the discrete-time model for the system seen by the controller can be written as

$$\mathbf{x}(k+1) = \underbrace{\begin{bmatrix} \mathbf{\Phi}_{\rm p} & \mathbf{\Gamma}_{\rm cp} \\ \mathbf{0} & 0 \end{bmatrix}}_{\mathbf{\Phi}} \mathbf{x}(k) + \underbrace{\begin{bmatrix} \mathbf{0} \\ \boldsymbol{\gamma} \end{bmatrix}}_{\mathbf{\Gamma}_{\rm c}} \boldsymbol{u}_{\rm c,ref}(k) + \underbrace{\begin{bmatrix} \mathbf{\Gamma}_{\rm gp} \\ 0 \end{bmatrix}}_{\mathbf{\Gamma}_{\rm g}} \boldsymbol{u}_{\rm g}(k)$$
$$\boldsymbol{i}_{\rm g}(k) = \underbrace{\begin{bmatrix} 1 & 0 & 0 & 0 \end{bmatrix}}_{\mathbf{C}_{\rm g}} \mathbf{x}(k) \tag{46}$$

where $\mathbf{x} = [\boldsymbol{i}_{\rm g}, \boldsymbol{i}_{\rm c}, \boldsymbol{u}_{\rm f}, \boldsymbol{u}_{\rm c}]^{\rm T}$ is the state vector. Since the computational delay (45) is included in the discrete-time model, the order of the system model (46) increases by one as compared to the model (42).

[3] In stationary coordinates, the computational delay is modeled as $\boldsymbol{u}_{\rm c}^{\rm s}(k+1) = \boldsymbol{u}_{\rm c,ref}^{\rm s}(k)$, where $\boldsymbol{u}_{\rm c,ref}^{\rm s}$ is the voltage reference for the PWM according to Fig. 1.

Appendix B
Feedback Controller and Reference Prefilter

To derive transfer functions $\boldsymbol{F}^{\rm i}(z)$ and $\boldsymbol{C}^{\rm i}(z)$ for integrator-based control, the observer (8) and the control law (5) are combined. First, the state-feedback gain $\mathbf{K}_{\rm fi} = [\boldsymbol{k}_{\rm a}, \mathbf{K}_{\rm b}]$ is split into gain $\boldsymbol{k}_{\rm a}$ for the measured state $\boldsymbol{i}_{\rm g}$ and gain $\mathbf{K}_{\rm b}$ for the estimated states $\hat{\mathbf{x}}_{\rm r}$. Then, the control law (5) is inserted in (8) and the resulting controller is written in a state-space form as

$$\begin{aligned} \mathbf{x}_{\rm c}(k+1) &= \mathbf{\Phi}_{\rm c}\mathbf{x}_{\rm c}(k) + \mathbf{\Gamma}_1\boldsymbol{i}_{\rm g}(k+1) + \mathbf{\Gamma}_2\boldsymbol{i}_{\rm g}(k) \\ &\quad + \mathbf{\Gamma}_3\boldsymbol{i}_{\rm g,ref}(k) \\ \boldsymbol{u}_{\rm c,ref}(k) &= -[\mathbf{K}_{\rm b}, -\boldsymbol{k}_{\rm i}]\mathbf{x}_{\rm c}(k) - \boldsymbol{k}_{\rm a}\boldsymbol{i}_{\rm g}(k) + \boldsymbol{k}_{\rm t}\boldsymbol{i}_{\rm g,ref}(k) \end{aligned} \tag{47}$$

where $\mathbf{x}_{\rm c} = [\hat{\mathbf{x}}_{\rm r}^{\rm T}, \boldsymbol{x}_{\rm i}]^{\rm T}$ is the state vector and

$$\mathbf{\Phi}_{\rm c} = \begin{bmatrix} \mathbf{\Phi}_{\rm bb} - \mathbf{K}_{\rm oi}\mathbf{\Phi}_{\rm ab} - \mathbf{\Gamma}_{\rm r}\mathbf{K}_{\rm b} & \mathbf{\Gamma}_{\rm r}\boldsymbol{k}_{\rm i} \\ \mathbf{0} & 1 \end{bmatrix} \qquad \mathbf{\Gamma}_1 = \begin{bmatrix} \mathbf{K}_{\rm oi} \\ 0 \end{bmatrix}$$
$$\mathbf{\Gamma}_2 = \begin{bmatrix} \mathbf{\Phi}_{\rm ba} - \mathbf{K}_{\rm oi}\boldsymbol{\phi}_{\rm aa} - \mathbf{\Gamma}_{\rm r}\boldsymbol{k}_{\rm a} \\ -1 \end{bmatrix} \qquad \mathbf{\Gamma}_3 = \begin{bmatrix} \mathbf{\Gamma}_{\rm r}\boldsymbol{k}_{\rm t} \\ 1 \end{bmatrix}. \tag{48}$$

In the z domain, the controller (47) can be written as

$$\begin{aligned} z\mathbf{x}_{\rm c}(z) &= \mathbf{\Phi}_{\rm c}\mathbf{x}_{\rm c}(z) + (z\mathbf{\Gamma}_1 + \mathbf{\Gamma}_2)\,\boldsymbol{i}_{\rm g}(z) + \mathbf{\Gamma}_3\boldsymbol{i}_{\rm g,ref}(z) \\ \boldsymbol{u}_{\rm c,ref}(z) &= -[\mathbf{K}_{\rm b}, -\boldsymbol{k}_{\rm i}]\mathbf{x}_{\rm c}(z) - \boldsymbol{k}_{\rm a}\boldsymbol{i}_{\rm g}(z) + \boldsymbol{k}_{\rm t}\boldsymbol{i}_{\rm g,ref}(z). \end{aligned} \tag{49}$$

If the controller is expressed as

$$\boldsymbol{u}_{\rm c,ref}(z) = \boldsymbol{C}^{\rm i}(z)[\boldsymbol{F}^{\rm i}(z)\boldsymbol{i}_{\rm g,ref}(z) - \boldsymbol{i}_{\rm g}(z)] \tag{50}$$

according to Fig. 3, the feedback controller is directly obtained from (48) and (49) as

$$\boldsymbol{C}^{\rm i}(z) = [\mathbf{K}_{\rm b}, -\boldsymbol{k}_{\rm i}](z\mathbf{I} - \mathbf{\Phi}_{\rm c})^{-1}(z\mathbf{\Gamma}_1 + \mathbf{\Gamma}_2) + \boldsymbol{k}_{\rm a} \tag{51}$$

and the reference prefilter as

$$\boldsymbol{F}^{\rm i}(z) = \frac{-[\mathbf{K}_{\rm b}, -\boldsymbol{k}_{\rm i}](z\mathbf{I} - \mathbf{\Phi}_{\rm c})^{-1}\mathbf{\Gamma}_3 + \boldsymbol{k}_{\rm t}}{\boldsymbol{C}^{\rm i}(z)}. \tag{52}$$

The transfer functions $\boldsymbol{F}^{\rm d}(z)$ and $\boldsymbol{C}^{\rm d}(z)$ for disturbance-observer-based control can be obtained in a similar way. The observer (12), disturbance state (13), and the control law (10) are combined. The state-feedback gain $\mathbf{K}_{\rm fd} = [\boldsymbol{k}_{\rm a}, \mathbf{K}_{\rm b}]$ is split into gain $\boldsymbol{k}_{\rm a}$ for the measured state $\boldsymbol{i}_{\rm g}$ and gain $\mathbf{K}_{\rm b}$ for the estimated states $\hat{\mathbf{x}}_{\rm r}$. Using (10), (12), and (13), the resulting state-space form of the controller becomes

$$\begin{aligned} \mathbf{x}_{\rm c}(k+1) &= \mathbf{\Phi}_{\rm c}\mathbf{x}_{\rm c}(k) + \mathbf{\Gamma}_1\boldsymbol{i}_{\rm g}(k+1) + \mathbf{\Gamma}_2\boldsymbol{i}_{\rm g}(k) \\ &\quad + \mathbf{\Gamma}_3\boldsymbol{i}_{\rm g,ref}(k) \\ \boldsymbol{u}_{\rm c,ref}(k) &= -[\mathbf{K}_{\rm b}, 1]\mathbf{x}_{\rm c}(k) - \boldsymbol{k}_{\rm a}\boldsymbol{i}_{\rm g}(k) + \boldsymbol{k}_{\rm f}\boldsymbol{i}_{\rm g,ref}(k) \end{aligned} \tag{53}$$

where $\mathbf{x}_{\rm c} = [\hat{\mathbf{x}}_{\rm r}^{\rm T}, \hat{\boldsymbol{w}}]^{\rm T}$ is the state vector and

$$\mathbf{\Phi}_{\rm c} = \begin{bmatrix} \mathbf{\Phi}_{\rm bb} - \mathbf{K}_{\rm od}\mathbf{\Phi}_{\rm ab} - \mathbf{\Gamma}_{\rm r}\mathbf{K}_{\rm b} & \mathbf{0} \\ -\boldsymbol{k}_{\rm w}\mathbf{\Phi}_{\rm ab} & 1 \end{bmatrix} \qquad \mathbf{\Gamma}_1 = \begin{bmatrix} \mathbf{K}_{\rm od} \\ \boldsymbol{k}_{\rm w} \end{bmatrix}$$
$$\mathbf{\Gamma}_2 = \begin{bmatrix} \mathbf{\Phi}_{\rm ba} - \mathbf{K}_{\rm od}\boldsymbol{\phi}_{\rm aa} - \mathbf{\Gamma}_{\rm r}\boldsymbol{k}_{\rm a} \\ -\boldsymbol{k}_{\rm w}\boldsymbol{\phi}_{\rm aa} \end{bmatrix} \qquad \mathbf{\Gamma}_3 = \begin{bmatrix} \mathbf{\Gamma}_{\rm r}\boldsymbol{k}_{\rm f} \\ 0 \end{bmatrix}. \tag{54}$$

In the z domain, the controller (53) is written as

$$\begin{aligned} z\mathbf{x}_{\mathrm{c}}(z) &= \mathbf{\Phi}_{\mathrm{c}}\mathbf{x}_{\mathrm{c}}(z) + (z\mathbf{\Gamma}_1 + \mathbf{\Gamma}_2)\boldsymbol{i}_{\mathrm{g}}(z) + \mathbf{\Gamma}_3\boldsymbol{i}_{\mathrm{g,ref}}(z) \\ \boldsymbol{u}_{\mathrm{c,ref}}(z) &= -[\mathbf{K}_{\mathrm{b}}, 1]\mathbf{x}_{\mathrm{c}}(z) - \boldsymbol{k}_{\mathrm{a}}\boldsymbol{i}_{\mathrm{g}}(z) + \boldsymbol{k}_{\mathrm{f}}\boldsymbol{i}_{\mathrm{g,ref}}(z). \end{aligned} \tag{55}$$

From (54) and (55), the feedback controller and the reference prefilter, respectively, become

$$\boldsymbol{C}^{\mathrm{d}}(z) = [\mathbf{K}_{\mathrm{b}}, 1](z\mathbf{I} - \mathbf{\Phi}_{\mathrm{c}})^{-1}(z\mathbf{\Gamma}_1 + \mathbf{\Gamma}_2) + \boldsymbol{k}_{\mathrm{a}} \tag{56}$$

$$\boldsymbol{F}^{\mathrm{d}}(z) = \frac{-[\mathbf{K}_{\mathrm{b}}, 1](z\mathbf{I} - \mathbf{\Phi}_{\mathrm{c}})^{-1}\mathbf{\Gamma}_3 + \boldsymbol{k}_{\mathrm{f}}}{\boldsymbol{C}^{\mathrm{d}}(z)}. \tag{57}$$

References

[1] M. Liserre, F. Blaabjerg, and S. Hansen, "Design and control of an LCL-filter-based three-phase active rectifier," *IEEE Trans. Ind. Appl.*, vol. 41, no. 5, pp. 1281–1291, Sep./Oct. 2005.

[2] J. Dannehl, C. Wessels, and F. W. Fuchs, "Limitations of voltage-oriented PI current control of grid-connected PWM rectifiers with LCL filters," *IEEE Trans. Ind. Electron.*, vol. 56, no. 2, pp. 380–388, Feb. 2009.

[3] D. N. Zmood, D. G. Holmes, and G. H. Bode, "Frequency-domain analysis of three-phase linear current regulators," *IEEE Trans. Ind. Appl.*, vol. 37, no. 2, pp. 601–610, Mar./Apr. 2001.

[4] J. G. Hwang, P. W. Lehn, and M. Winkelnkemper, "A generalized class of stationary frame-current controllers for grid-connected AC–DC converters," *IEEE Trans. Power Del.*, vol. 25, no. 4, pp. 2742–2751, Oct. 2010.

[5] D. N. Zmood and D. G. Holmes, "Stationary frame current regulation of PWM inverters with zero steady-state error," *IEEE Trans. Power Electron.*, vol. 18, no. 3, pp. 814–822, May 2003.

[6] M. Liserre, R. Teodorescu, and F. Blaabjerg, "Stability of photovoltaic and wind turbine grid-connected inverters for a large set of grid impedance values," *IEEE Trans. Power Electron.*, vol. 21, no. 1, pp. 263–272, Jan. 2006.

[7] I. J. Gabe, V. F. Montagner, and H. Pinheiro, "Design and implementation of a robust current controller for VSI connected to the grid through an LCL filter," *IEEE Trans. Power Electron.*, vol. 24, no. 6, pp. 1444–1452, Jun. 2009.

[8] J. Kukkola, M. Hinkkanen, and K. Zenger, "Observer-based state-space current controller for a grid converter equipped with an LCL filter: Analytical method for direct discrete-time design," *IEEE Trans. Ind. Appl.*, vol. 51, no. 5, pp. 4079–4090, Sep./Oct. 2015.

[9] D. Pérez-Estévez, J. Doval-Gandoy, A. G. Yepes, and O. López, "Positive- and negative-sequence current controller with direct discrete-time pole placement for grid-tied converters with LCL filter," *IEEE Trans. Power Electron.*, vol. 32, no. 9, pp. 7207–7221, Sep. 2017.

[10] F. M. M. Rahman, U. Riaz, J. Kukkola, M. Routimo, and M. Hinkkanen, "Observer-based current control for converters with an LCL filter: Robust design for weak grids," in *Proc. IEEE Int. Symp. Sensorless Control Elect. Drives*, Helsinki, Finland, Sep. 2018, pp. 36–41.

[11] V. Miskovic, V. Blasko, T. M. Jahns, A. H. C. Smith, and C. Romenesko, "Observer-based active damping of LCL resonance in grid-connected voltage source converters," *IEEE Trans. Ind. Appl.*, vol. 50, no. 6, pp. 3977–3985, Nov./Dec. 2014.

[12] J. Dannehl, F. W. Fuchs, and P. B. Thøgersen, "PI state space current control of grid-connected PWM converters with LCL filters," *IEEE Trans. Power Electron.*, vol. 25, no. 9, pp. 2320–2330, Sep. 2010.

[13] C. A. Busada, S. G. Jorge, and J. A. Solsona, "Full-state feedback equivalent controller for active damping in LCL-filtered grid-connected inverters using a reduced number of sensors," *IEEE Trans. Ind. Electron.*, vol. 62, no. 10, pp. 5993–6002, Oct. 2015.

[14] J. Kukkola and M. Hinkkanen, "Observer-based state-space current control for a three-phase grid-connected converter equipped with an LCL filter," *IEEE Trans. Ind. Appl.*, vol. 50, no. 4, pp. 2700–2709, Jul./Aug. 2014.

[15] Y. Tang, P. C. Loh, P. Wang, F. H. Choo, F. Gao, and F. Blaabjerg, "Generalized design of high performance shunt active power filter with output LCL filter," *IEEE Trans. Ind. Electron.*, vol. 59, no. 3, pp. 1443–1452, Mar. 2012.

[16] J. Dannehl, F. W. Fuchs, S. Hansen, and P. B. Thøgersen, "Investigation of active damping approaches for PI-based current control of grid-connected pulse width modulation converters with LCL filters," *IEEE Trans. Ind. Appl.*, vol. 46, no. 4, pp. 1509–1517, Jul. 2010.

[17] X. Wang, F. Blaabjerg, and P. C. Loh, "Grid-current-feedback active damping for LCL resonance in grid-connected voltage-source converters," *IEEE Trans. Power Electron.*, vol. 31, no. 1, pp. 213–223, Jan. 2016.

[18] C. Zou, B. Liu, S. Duan, and R. Li, "Influence of delay on system stability and delay optimization of grid-connected inverters with LCL filter," *IEEE Trans. Ind. Informat.*, vol. 10, no. 3, pp. 1775–1784, Aug. 2014.

[19] S. G. Parker, B. P. McGrath, and D. G. Holmes, "Regions of active damping control for LCL filters," *IEEE Trans. Ind. Appl.*, vol. 50, no. 1, pp. 424–432, Jan./Feb. 2014.

[20] Z. Xin, X. Wang, P. C. Loh, and F. Blaabjerg, "Grid-current-feedback control for LCL-filtered grid converters with enhanced stability," *IEEE Trans. Power Electron.*, vol. 32, no. 4, pp. 3216–3228, Apr. 2017.

[21] S. Alepuz, S. Busquets-Monge, J. Bordonau, J. A. Martinez-Velasco, C. A. Silva, J. Pontt, and J. Rodriguez, "Control strategies based on symmetrical components for grid-connected converters under voltage dips," *IEEE Trans. Ind. Electron.*, vol. 56, no. 6, pp. 2162–2173, Jun. 2009.

[22] F. Huerta, D. Pizarro, S. Cóbreces, F. J. Rodriguez, C. Girón, and A. Rodriguez, "LQG servo controller for the current control of LCL grid-connected voltage-source converters," *IEEE Trans. Ind. Electron.*, vol. 59, no. 11, pp. 4272–4284, Nov. 2012.

[23] E. Wu and P. W. Lehn, "Digital current control of a voltage source converter with active damping of LCL resonance," *IEEE Trans. Power Electron.*, vol. 21, no. 5, pp. 1364–1373, Sep. 2006.

[24] R. Turner, S. Walton, and R. Duke, "Robust high-performance inverter control using discrete direct-design pole placement," *IEEE Trans. Ind. Electron.*, vol. 58, no. 1, pp. 348–357, Jan. 2011.

[25] G. F. Franklin, D. Powell, and M. L. Workman, *Digital Control of Dynamic Systems*, 3rd ed. Menlo Park, CA: Addison-Wesley, 1998.

[26] W. Chen, J. Yang, L. Guo, and S. Li, "Disturbance-observer-based control and related methods—An overview," *IEEE Trans. Ind. Electron.*, vol. 63, no. 2, pp. 1083–1095, Feb. 2016.

[27] J. Liu, W. Wu, H. S. Chung, and F. Blaabjerg, "Disturbance observer-based adaptive current control with self-learning ability to improve the grid-injected current for LCL-filtered grid-connected inverter," *IEEE Access*, vol. 7, pp. 105 376–105 390, Aug. 2019.

[28] A. Al-Durra and R. Errouissi, "Robust feedback-linearization technique for grid-tied LCL filter systems using disturbance estimation," *IEEE Trans. Ind. Appl.*, vol. 55, no. 3, pp. 3185–3197, May 2019.

[29] H. Akagi, E. H. Watanabe, and M. Aredes, *Instantaneous power theory and applications to power conditioning*. Hoboken, NJ, USA: John Wiley & Sons, 2007.

[30] Y. Peng, D. Vrancic, and R. Hanus, "Anti-windup, bumpless, and conditioned transfer techniques for PID controllers," *IEEE Control Syst. Mag.*, vol. 16, no. 4, pp. 48–57, Aug. 1996.

[31] K. J. Åström and B. Wittenmark, *Computer-controlled systems: Theory and Design*, 3rd ed. Upper Saddle River, NJ, USA: Prentice Hall, 1997.

[32] S. Skogestad and I. Postlethwaite, *Multivarialbe Feedback Control: Analysis and Design*. West Sussex, England: John Wiley and Sons, 1996.

[33] V. Kaura and V. Blasko, "Operation of a phase locked loop system under distorted utility conditions," *IEEE Trans. Ind. Appl.*, vol. 33, no. 1, pp. 58–63, Jan./Feb. 1997.

F. M. Mahafugur Rahman (S'20) received the B.Sc.(Tech.) degree in electrical and electronic engineering from the Chittagong University of Engineering and Technology, Chittagong, Bangladesh, in 2011. He received the M.Sc.(Tech.) degree in electronics and electrical engineering from the Aalto University, Espoo, Finland, in 2016, where he is currently working toward the D.Sc.(Tech.) degree in electrical engineering.

His research interests include control of grid-connected converters.

Ville Pirsto received the B.Sc. (Tech.) and M.Sc. (Tech.) degrees in electrical engineering from the Aalto University, Espoo, Finland, in 2017 and 2019, respectively, where he is currently working toward the D.Sc. (Tech.) in electrical engineering.

His current research focuses on grid-connected converters.

Jarno Kukkola received the B.Sc. (Tech.), M.Sc. (Tech.), and D.Sc. (Tech.) degrees in electrical engineering from the Aalto University, Espoo, Finland, in 2010, 2012, and 2017, respectively.

He is currently a Postdoctoral Researcher with the School of Electrical Engineering, Aalto University, Espoo, Finland. His research interests include control systems and grid-connected converters.

Marko Hinkkanen (M'06–SM'13) received the M.Sc.(Eng.) and D.Sc.(Tech.) degrees in electrical engineering from the Helsinki University of Technology, Espoo, Finland, in 2000 and 2004, respectively.

He is currently an Associate Professor with the School of Electrical Engineering, Aalto University, Espoo, Finland. His research interests include control systems, electric drives, and power converters.

Dr. Hinkkanen was the corecipient of the 2016 International Conference on Electrical Machines (ICEM) Brian J. Chalmers Best Paper Award, the 2016 and 2018 IEEE Industry Applications Society Industrial Drives Committee Best Paper Awards, and the 2020 SEMIKRON Innovation Award. He is an Associate Editor for the IEEE TRANSACTIONS ON ENERGY CONVERSION and the *IET Electric Power Applications*.

Diego Pérez-Estévez (S'15) received the M.Sc. and the Ph.D. degrees from the University of Vigo, Vigo, Spain, in 2014 and 2019, respectively.

Since 2014, he has been with the Applied Power Electronics Technology Research Group. His research interests include control of grid-connected converters and distributed power generation systems.

Jesús Doval-Gandoy (M'99) received the M.S. and Ph.D. degrees in electrical engineering from the Polytechnic University of Madrid, Madrid, Spain, and from the University of Vigo, Vigo, Spain, in 1991 and 1999, respectively. He is a Professor and the Head of the Applied Power Electronics Technology Research Group (APET), University of Vigo.

His research interests are in the areas of ac power conversion.